



HAL
open science

Electrodeposition of arrays of Ru, Pt, and PtRu Alloy 1D metallic nanostructures

Alexandre Ponrouch, Sébastien Garbarino, Stéphanie Pronovost, Pierre-Louis Taberna, Patrice Simon, Daniel Guay

► **To cite this version:**

Alexandre Ponrouch, Sébastien Garbarino, Stéphanie Pronovost, Pierre-Louis Taberna, Patrice Simon, et al.. Electrodeposition of arrays of Ru, Pt, and PtRu Alloy 1D metallic nanostructures. *Journal of The Electrochemical Society*, 2010, 157 (3), pp.K59-K65. 10.1149/1.3276500 . hal-03557573

HAL Id: hal-03557573

<https://hal.science/hal-03557573>

Submitted on 4 Feb 2022

HAL is a multi-disciplinary open access archive for the deposit and dissemination of scientific research documents, whether they are published or not. The documents may come from teaching and research institutions in France or abroad, or from public or private research centers.

L'archive ouverte pluridisciplinaire **HAL**, est destinée au dépôt et à la diffusion de documents scientifiques de niveau recherche, publiés ou non, émanant des établissements d'enseignement et de recherche français ou étrangers, des laboratoires publics ou privés.



Open Archive Toulouse Archive Ouverte (OATAO)

OATAO is an open access repository that collects the work of Toulouse researchers and makes it freely available over the web where possible.

This is an author-deposited version published in: <http://oatao.univ-toulouse.fr/>
Eprints ID: 3878

To link to this article: DOI: 10.1149/1.3276500
URL: <http://dx.doi.org/10.1149/1.3276500>

To cite this version: Ponrouch, Alexandre and Garbarino, Sébastien and Pronovost, Stéphanie and Taberna, Pierre-Louis and Simon, Patrice and Guay, Daniel (2010) *Electrodeposition of Arrays of Ru, Pt, and PtRu Alloy 1D Metallic Nanostructures*. Journal of The Electrochemical Society (JES), vol. 157 (n° 3). pp. K59-K65. ISSN 0013-4651

Any correspondence concerning this service should be sent to the repository administrator: staff-oatao@inp-toulouse.fr

Electrodeposition of Arrays of Ru, Pt, and PtRu Alloy 1D Metallic Nanostructures

Alexandre Ponrouch,^{a,*} Sébastien Garbarino,^{a,*} Stéphanie Pronovost,^a
Pierre-Louis Taberna,^b Patrice Simon,^{b,**} and Daniel Guay^{a,*,*,z}

^aInstitut National de la Recherche Scientifique-Énergie, Matériaux et Télécommunications, Varennes,
Québec J3X 1S2, Canada

^bCentre Interuniversitaire de Recherche et d'Ingénierie des Matériaux, UMR CNRS 5085, Université Paul
Sabatier, Toulouse 31062, France

Arrays of Ru, Pt, and PtRu one dimensional (1D) nanowires (NWs) and nanotubes (NTs) were prepared by electrodeposition through the porous structure of an anodic aluminum oxide (AAO) membrane. In each case, micrometer-long NW and NT were formed with an outer diameter of ca. 200 nm, close to the interior diameter of the porous AAO membrane. Arrays of NW and NT can be formed by varying the metallic salt concentration, the applied potential, and the conductivity of the electrolyte. The Ru and Pt deposition rates were measured in the various deposition conditions, using an electrochemical quartz crystal microbalance. The mechanisms responsible for the formation of Ru and Pt NW and NT are discussed based on the observed deposition rates and models found in the literature. Finally, it is shown that arrays of PtRu alloy NT and NW can be readily prepared and their compositions can be varied over the whole compositional range by changing the metallic salt concentration of the electrodeposition bath.

Nanotubes (NTs) and nanowires (NWs) have attracted significant interest as a result of their peculiar properties, imposed by the anisotropy of their one-dimensional (1D) geometry.¹⁻⁴ These 1D motifs (wherein two of the three structural dimensions are smaller than a few hundreds of nanometers) are of interest for several applications such as biotechnology, catalysis, drug delivery, electronics, energy storage, magnetic recording device, nanodevices, nanotemplating, optoelectronics, photovoltaics, photoelectrochemistry, and sensing.⁵⁻¹⁷ They have been prepared by various methods including vapor-phase synthesis,^{18,19} solution-phase methods based on capping reagents,^{20,21} and template-assisted method.²²⁻²⁴ Since it was first reported by Frazier et al.,²² the template-assisted method has attracted much attention due to its simplicity and versatility.

Metallic 1D nanostructures have intrinsically interesting optical properties and several studies in the literature have made use of them, including sensing and imaging. In comparison, there are fewer papers dealing with the electrocatalytic properties of the metallic 1D nanostructures. Recently, supportless Pt,^{3,25} Ag,²⁵ and Au²⁵ have been investigated for the oxygen reduction reaction. Also, in recent papers from our group,²⁶⁻²⁹ we showed that arrays of Ru, Pt, and PtRu NTs and NWs prepared by electrochemical deposition via the template-assisted method with a porous anodic aluminum oxide (AAO) membrane have interesting electrocatalytic properties for reactions that are of interest for the development of effective fuel cell catalysts.

Platinum is considered one of the best (if not the best) electrocatalysts for polymer electrolyte fuel cell applications. It shows high electrocatalytic activity for the hydrogen oxidation and the oxygen reduction reactions. Recently, a few reports have appeared describing how a micrometer-long metallic Pt 1D nanostructure can be prepared.^{24,25,29} However, it is well known that the electrocatalytic properties and the long-term resistance of Pt can be further improved by alloying with another element. For example, it is known that PtRu exhibits improved tolerance to CO poisoning and that alloying of Pt can also improve the oxygen reduction kinetics.³⁰ For these reasons, it is of interest to develop methods of preparing an alloyed, Pt-based, micrometer-long, metallic 1D nanostructure to be

able to study how the electrocatalytic activity of these anisotropic structures is modified with respect to nanoparticles.

In this paper, we report on the preparation of an array of PtRu alloy with micrometer-long 1D nanostructures. These arrays are prepared by coelectrodeposition through an AAO membrane, using an electroplating bath that contains Pt⁴⁺ and Ru³⁺ metallic ions. We show that the composition of these 1D nanostructures can be varied by controlling the composition of the electroplating bath. The Ru and Pt deposition rate is measured, and we show that the composition of the PtRu alloy can be assessed from the deposition rate of both metals. Finally, the NW and NT growth mechanisms are discussed in the context of the models proposed by Fukunaka et al. (coevolution of hydrogen),³¹ Xiao et al.,³² and Cho and Lee³³ (limited mass transport).

Experimental

Ru, Pt, and PtRu were electroplated on Ti substrates prepared as previously described.²⁶ Three different types of deposit were obtained, namely, films, NWs, and NTs. The films were obtained by deposition on a bare Ti substrate. By contrast, NWs and NTs were prepared by electrochemical deposition through the porous structure of an AAO membrane (Anodisc 25, Whatman International Ltd.). The experimental setup used was already described in detail elsewhere.²⁶ No pretreatment (metallization or functionalization) was performed on the AAO membrane, and the NWs and NTs were grown on the metallic film that was first deposited in the gap between the Ti substrate and the porous membrane. The electroplating solution consisted of HCl (10 mM), and the metallic salts were Na₂PtCl₆·xH₂O and RuCl₃·6H₂O (Alfa Aesar). In some cases, KCl (0.1 M) was added to the plating bath. All depositions were performed in potentiostatic mode using a Solartron SI 1287 potentiostat-galvanostat, with all deposition potentials (V_{dep}) referred to the saturated calomel electrode (SCE) scale. After electrodeposition, the working electrode was removed from the electrolyte and, in the case of NW and NT deposits, the AAO membrane was dissolved by immersion in 1 M NaOH for 2 h at room temperature.

Gold-plated crystals (9 MHz AT-cut) were used for the electrochemical quartz crystal microbalance (EQCM) experiments. The calibration constant determined by Pb deposition was 1.15 ng · Hz⁻¹, close to the theoretical value calculated from the Sauerbrey equation.³⁴ The Ru and Pt deposition rates were determined by first electroplating these metals (-0.4 V for 300 s) on the

* Electrochemical Society Student Member.

** Electrochemical Society Active Member.

^z E-mail: guay@emt.inrs.ca

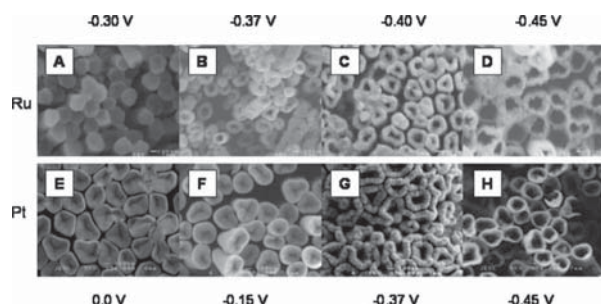


Figure 1. SEM micrographs for [(A)-(D)] Ru and [(E)-(H)] Pt electrochemically deposited through an AAO membrane. (A)-(D) plating bath: 5 mM $\text{RuCl}_3 \cdot 6\text{H}_2\text{O}$, 10 mM HCl, 0.1 M KCl, and $T = 50^\circ\text{C}$; (E)-(H) plating bath: 5 mM $\text{Na}_2\text{PtCl}_6 \cdot x\text{H}_2\text{O}$, 10 mM HCl, and $T = 25^\circ\text{C}$.

bare Au-coated crystals and then adjusting the electrode potential to the desired value. This was done to prevent the deposition of Ru and Pt on a foreign metal (Au in this case) as well as to ensure a constant initial roughness factor of the substrate. The deposition rate was calculated by ignoring the initial mass variation, and stationary deposition rates were obtained in all cases. In all cases, the surface area of the crystal was 0.2 cm^2 .

The conductivity of the plating bath was measured with an Oakton CON 11 standard conductivity meter. The morphology of the deposits was observed using a scanning electron microscope (SEM, JSM-6300F, JEOL). The structure and crystallite size of the deposits were obtained by X-ray diffraction (XRD) using a Bruker D8 Advance with $\text{Cu K}\alpha$ at 1.5418 \AA . The diffraction patterns were achieved in the Bragg-Brentano $\theta/2\theta$ configuration, and structure refinement was performed according to the Rietveld method³⁵ using GSAS and EXPGUI software.^{36,37}

Results and Discussion

Pt and Ru nanostructures.—Effect of deposition potential.—Pt and Ru were electrodeposited through an AAO membrane under the following electroplating conditions: (i) For Ru, the plating bath consisted of 5 mM $\text{RuCl}_3 \cdot 6\text{H}_2\text{O}$, 10 mM HCl, 0.1 M KCl, and $T = 50^\circ\text{C}$. (ii) For Pt, the plating bath was 5 mM $\text{Na}_2\text{PtCl}_6 \cdot x\text{H}_2\text{O}$, 10 mM HCl, and $T = 25^\circ\text{C}$. For Ru, the deposition potential, V_{dep} , was varied from -0.30 to -0.45 V , while for Pt it was changed from 0.00 to -0.45 V . The effect of V_{dep} on the morphology of Ru and Pt deposited through an AAO membrane is depicted in Fig. 1 through a series of scanning electron microscopy micrographs. In both cases, NWs are achieved for $V_{\text{dep}} \geq -0.3 \text{ V}$, while NTs are obtained for $V_{\text{dep}} \leq -0.3 \text{ V}$. Moreover, the characteristic dimensions of the Ru and Pt NTs, namely, the wall thickness (W_l) and the internal pore diameter (D_l), vary with V_{dep} . For example, for Ru and Pt NT, D_l increases from 65 to 210 nm and from 140 to 235 nm, respectively, while, W_l decreases from 85 to 40 nm and from 95 to 35 nm, respectively, as V_{dep} varies from -0.37 to -0.45 V .

The deposition rates (defined as moles of metal deposited per unit of time) for Ru and Pt, in similar plating bath conditions as that shown in Fig. 1, were extracted from EQCM analyses of films deposited at different V_{dep} values, and the results are displayed in Fig. 2. Clearly, the evolution of the deposition rate vs V_{dep} is quite different for these two metals. The deposition rate for Ru at 50°C is extremely low ($< 1 \times 10^{-11} \text{ mol s}^{-1}$) for $V_{\text{dep}} \geq \text{ca. } -0.30 \text{ V}$, and increases drastically as V_{dep} is made more cathodic (kinetic control). The same behavior is observed at lower temperature ($T = 25^\circ\text{C}$), although the deposition rate values are lower. For both temperatures, no limiting value of the deposition rate is observed, which indicates that deposition is not limited by the diffusion of electroactive species toward the electrode surface. By contrast, the deposition rate of Pt increases as V_{dep} decreased from 0.0 to -0.3 V (kinetic control),

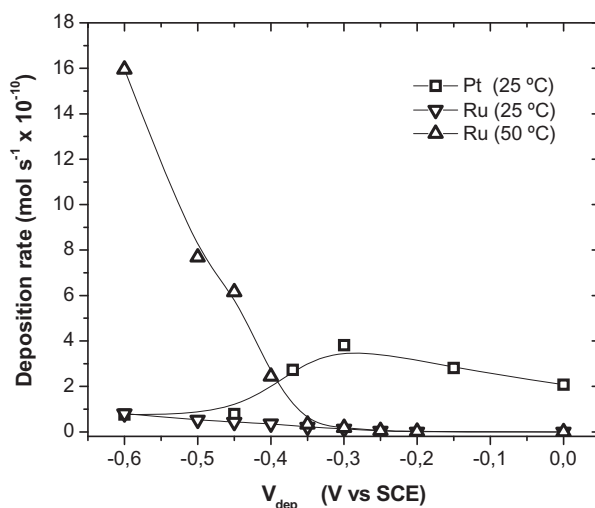


Figure 2. Deposition rate of Ru and Pt as a function of V_{dep} in similar plating bath conditions as in Fig. 1. The temperature of the solutions is indicated.

and then decreases as V_{dep} is made more negative (from -0.30 to -0.45 V). For $V_{\text{dep}} \leq \text{ca. } -0.45 \text{ V}$, the Pt deposition rate reaches a constant value of $\text{ca. } 0.75 \times 10^{-10} \text{ mol s}^{-1}$.

The evolution of the Ru deposition rate with V_{dep} is not surprising because it was already reported that the coevolution of hydrogen affects the deposition of Ru,³⁸ probably due to the formation of ruthenium hydroxide complexes, which play a key role as an intermediate species during the deposition process. Nevertheless, the deposition of Ru is not limited by diffusion in the deposition potential range applied in this study. This is proven to be important in the following.

In contrast, the evolution of the Pt deposition rate with V_{dep} follows more closely the expected trend, namely, an increase in the deposition rate as V_{dep} is cathodically shifted from the equilibrium deposition potential of platinum (kinetically controlled deposition). For large cathodic overpotentials (ca. $V_{\text{dep}} < -0.30 \text{ V}$), the Pt deposition rate decreases and deviates from the “ideal” behavior (constant deposition rate) expected as V_{dep} reaches the potential region where the growth of the film is limited by the diffusion of Pt^{4+} species to the electrode surface. This is because, in our experimental conditions, hydrogen evolution starts at ca. -0.3 V and may cause a chemical precipitation of Pt in the vicinity of the electrode, thereby causing a local reduction of the Pt^{4+} concentration.³⁹ Also, for $V_{\text{dep}} \leq -0.30 \text{ V}$, hydrogen evolution may further limit the accessibility of the electrode surface to Pt^{4+} species by reducing the effective surface area between the electrode and the electrolyte. Nevertheless, in this potential range ($V_{\text{dep}} < -0.30 \text{ V}$), the growth of the Pt film is limited by the diffusion of Pt^{4+} species to the electrode surface.

Influence of metallic salt concentration.—The equilibrium hydrogen evolution potential is ca. -0.3 V in our experimental conditions, and metal deposition at a very cathodic potential occurs simultaneously with hydrogen evolution. This was already shown to dramatically modify the concentration of $[\text{Pt}^{4+}]$ in the vicinity of the surface electrode. To assess how mass transport limitations can affect the morphology of the deposit in the absence of hydrogen evolution, the $[\text{Pt}^{4+}]$ concentration was varied and electrodeposition was performed at -0.15 V . For $[\text{Na}_2\text{PtCl}_6] = 0.5$ and 1.0 mM , the Pt deposition rates are $0.30 \pm 0.07 \times 10^{-10}$ and $0.40 \pm 0.07 \times 10^{-10} \text{ mol s}^{-1}$, respectively, and are almost independent of the deposition potential for $-0.3 \leq V_{\text{dep}} \leq 0.0 \text{ V}$ (data not shown). This suggests that at such low Na_2PtCl_6 concentration, Pt deposition is effectively limited by the diffusion of Pt^{4+} species to the substrate.

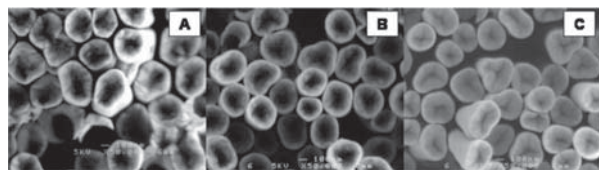


Figure 3. SEM micrographs for Pt electrochemically deposited through an AAO membrane at $V_{\text{dep}} = -0.15$ V: (A) 0.5, (B) 1, and (C) 5 mM Na_2PtCl_6 . In all cases, $Q_d = 40 \text{ C cm}^{-2}$.

SEM micrographs of Pt nanostructures obtained from 0.5, 1.0, and 5.0 mM solutions of Na_2PtCl_6 are shown in Fig. 3A-C, respectively. Pt NTs are obtained for $[\text{Na}_2\text{PtCl}_6] = 0.5$ and 1.0 mM solution, while Pt NWs are formed with $[\text{Na}_2\text{PtCl}_6] = 5$ mM solution. Therefore, Pt NTs can be prepared at -0.15 V, in the absence of hydrogen, if the Na_2PtCl_6 concentration is sufficiently reduced.

Figure 4 shows the corresponding XRD patterns for Pt nanostructures depicted in Fig. 3A-C ($V_{\text{dep}} = -0.15$ V, whereas $[\text{Pt}^{4+}]$ in solution is varied from 0.5 to 5.0 mM). The deposition charge density, Q_d , was kept constant at $40 \text{ C} \times \text{cm}^{-2}$ and at least 10 μm long NTs and NWs were grown in each case. All the peaks can be indexed to the hexagonal phase of Ti (substrate) and face-centered cubic (fcc) Pt, indicating that metallic Pt is formed. The crystallite sizes were extracted from the XRD patterns by performing a Rietveld refinement analysis. The Pt crystallite sizes decrease from 16 to 7 nm as the concentration of Pt^{4+} in solution increases from 0.5 (NTs) to 5.0 mM (NWs). It seems straightforward to conclude that a low Pt salt concentration limits the number of nucleation sites for Pt growth inside the confined pore of an AAO membrane and leads to larger crystallites.

Two hypotheses have been proposed in the literature to explain the growth of NTs inside a porous AAO membrane: (i) Fukunaka et al.³¹ suggested that concurrent gas evolution (hydrogen) during metal deposition would limit the accessibility of ionic species to the inside of the pores of the AAO membrane, and hence limit the metal deposition to regions that are close to the pore wall. This hypothesis was further investigated by Philippe and Michler⁴⁰ and is consistent with some recent reports suggesting that concurrent gas evolution (hydrogen) and metal electrodeposition have an effect on the structure of the deposit.^{41,42} (ii) Xiao et al.³² and Cho and Lee³³ suggested that fast, rate-limiting nucleation on the surface of the pore

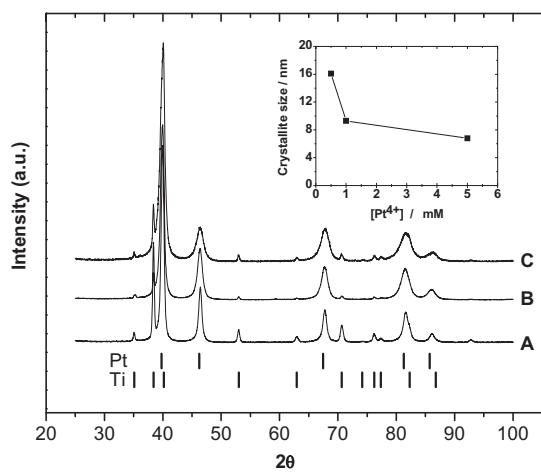


Figure 4. XRD patterns for Pt electrochemically deposited through an AAO membrane at $V_{\text{dep}} = -0.15$ V and $Q_d = 40 \text{ C cm}^{-2}$. The Na_2PtCl_6 concentration was (A) 0.5, (B) 1.0, and (C) 5.0 mM. The inset depicts the evolution of the crystallite size with $[\text{Na}_2\text{PtCl}_6]$.

walls would lead to competition between wall nucleation and diffusion-controlled pore filling as a function of the overall reaction rate. Thus, NT formation would result from a high deposition rate and a low ionic diffusion inside the porous structure of the membrane.

For Pt deposition, the model of Xiao et al.³² and Cho and Lee³³ appeared to be valid in the potential region where hydrogen evolution does not occur. Taking into account the geometrical dimensions of the pores of the AAO membrane (290 nm diameter and 60 μm length), ca. 2.0×10^{-18} , 4.0×10^{-18} , and 2.0×10^{-17} mol of Pt^{4+} are initially present in a single pore for 0.5, 1, and 5 mM Na_2PtCl_6 solutions, respectively. This would yield 0.27, 0.54, and 2.70 nm long Pt NWs if an inward flux of Pt^{4+} does not settle in during the growth process (the Pt NWs and NTs are a micrometer long). Therefore, Pt growth through an AAO membrane is rapidly controlled by the diffusion of Pt^{4+} through the pore of the membrane. As shown above, for $[\text{Pt}^{4+}] = 0.5$ and 1.0 mM, the deposition rate is a factor of 10 smaller than for $[\text{Pt}^{4+}] = 5.0$ mM, and limiting the Pt^{4+} mass transport is critical to favor the formation of Pt NTs. In the potential region where hydrogen evolution occurs, i.e., from -0.3 to -0.45 V, the Pt deposition rate decreased, which could suggest that the limited diffusion of Pt^{4+} to the growing Pt surface could be responsible for the formation of Pt NTs. However, at $V_{\text{dep}} = -0.37$ V, the Pt deposition rate is almost identical to that at $V_{\text{dep}} = -0.15$ V (see Fig. 2), where hydrogen evolution does not occur. This points to the fact that hydrogen evolution (at $V_{\text{dep}} \leq -0.30$ V) is also important in the mechanisms that yield to the formation of Pt NT.

For Ru, the variation of the deposition rate with V_{dep} observed in Fig. 2 is not compatible with the NT growth mechanisms model proposed by Xiao et al.³² and Cho and Lee³³ because the deposition rate is not limited by diffusion. Instead, the deposition rate of Ru increases steadily as V_{dep} is made more cathodic. In these deposition conditions, the NT growth mechanism suggested by Fukunaka et al.³¹ might prevail for Ru NT formation.

There are several important differences between this work and the previous ones. First, in most of the previous studies, the growth of NTs was performed on a gold-coated AAO membrane, with the gold coating making an annular shape at the pore basis of the membrane.^{31,32,40,43} A similar strategy was used elsewhere to grow an array of Pt NT using silver instead of gold.⁴⁴ This conductive annular base might initiate the nucleation at the circumference of the pore thanks to the well-known “tip effect.”^{45,46} This is not the case here because both Pt and Ru NTs were grown on a Pt and a Ru underlayer that filled the gap between the substrate and the AAO template. Also, this study differs from the works of Xiao et al.,³² Cho and Lee,³³ and Martin et al.^{23,43} as no pretreatment (metallization or functionalization) was necessary to obtain NTs. Furthermore, in contrast with Ref. 23, 32, and 33, the nanostructures formed with our setup remain in the form of NTs even for a long deposition time, allowing us to synthesize NTs of about 60 μm length (imposed by the thickness of the AAO membrane). This represents an aspect ratio of about 200, considering the average external diameter of these structures, at ca. 300 nm.

Influence of supporting electrolyte.— The concentration of Pt^{4+} ions in the precursor solution strongly influences the deposition rate and the nanostructure of the resulting deposit, but other factors turn out to be equally important such as the supporting electrolyte concentration. Figure 5 shows the SEM micrographs of Pt nanostructures deposited at -0.15 V in 1 mM Na_2PtCl_6 plating bath. Pt NTs are achieved in a KCl-free solution (Fig. 5A), while Pt NWs are obtained by the addition of 0.1 M KCl (Fig. 5B). The conductivity of the electrolyte linearly increases from 4.3 to 17.0 mS cm^{-1} as $[\text{KCl}]$ is varied from 0 to 0.1 M. Therefore, it seems obvious that the conductivity of the electrolyte is also an important parameter for the formation of NTs. A possible explanation is based on previous studies by Oldham⁴⁷ and Amatore et al.,⁴⁸ which showed that the resistance along the diameter of a disk microelectrode embedded in an

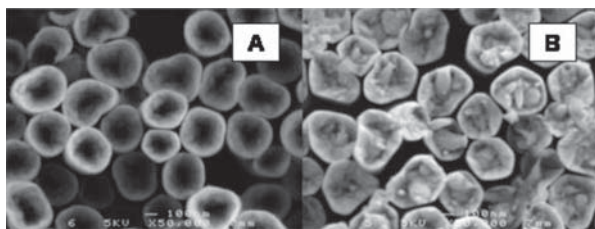


Figure 5. SEM micrographs for Pt electrochemically deposited through an AAO membrane at $V_{\text{dep}} = -0.15$ V, with $[\text{Na}_2\text{PtCl}_6] = 1$ mM and $[\text{HCl}] = 10$ mM: (A) without KCl and (B) with 0.1 M KCl. In all cases, $Q_d = 40$ C cm^{-2} .

insulator is not uniform over the disk surface. Indeed, the resistance decreases from the center to the outer diameter of the disk, resulting in a higher current density at the edge. It is straightforward to compare the surface resistance behavior of a disk microelectrode embedded in an insulator with that of an NW (or NT) that is growing inside the pore of an insulating AAO membrane. This inhomogeneous current density distribution was dependent on the overall system resistance.⁴⁸ Thus, the fact that different morphologies (NW or NT) were grown at fixed V_{dep} and $[\text{Pt}^{4+}]$ depending on the conductivity of the electrolyte results from an inhomogeneous distribution of equipotential lines as the KCl concentration is decreased. This could also explain why the nucleation is initiated at the edges of the growing disk, resulting in inverse conic top end Pt NWs (cf. Fig. 1E and F) for deposition under kinetic control. For low salt concentration where the growth mechanism is under diffusion-controlled conditions, this effect could further help the growth of NTs (cf. Fig. 3A and B).

Influence of the OCP period after deposition.— In Fig. 6, Pt nanostructures were deposited through an AAO membrane at -0.15 V in a 0.5 mM Na_2PtCl_6 , KCl-free plating bath. Pt NTs were obtained by pulling out the electrode immediately after Pt deposition (Fig. 6A), whereas Pt NWs were achieved in the same deposition conditions with the electrode left for 5 h at open-circuit potential (OCP) in the plating bath after deposition (Fig. 6B). The morphology of such Pt NWs differs from that of NWs displayed in Fig. 1 and 3. Indeed, the top end of these former NWs presents a dense and smooth circumference, while the center is very rough, porous, and tip shape (cf. Fig. 6B). As evidenced in Fig. 6C, damaged Pt NWs could be observed. Interestingly, the morphology observed in these damaged regions is reminiscent of the Pt NTs previously observed, suggesting that the mechanisms responsible for the rough structure observed at the top of the Pt nanostructures are different from those previously described. In each case, the composition of the deposit was checked by energy-dispersive X-ray analysis (EDS) and no trace of impurities was detected.

A combined EQCM and OCP study of Pt deposition during the latent period at the end of the electrodeposition process was undertaken to better understand the processes responsible for the previous observations. In Fig. 7A, the evolution of the OCP following Pt

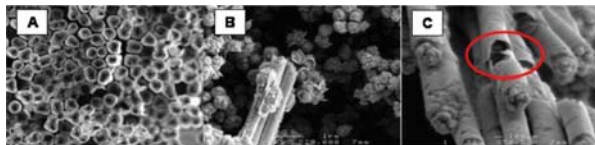


Figure 6. (Color online) SEM micrographs for Pt electrochemically deposited through an AAO membrane at -0.15 V in a 0.5 mM Na_2PtCl_6 , KCl-free plating bath. (A) Electrode removed immediately from the electroplating solution and rinsed with deionized water. [(B) and (C)] Electrode left for 5 h in the electroplating solution under OCP.

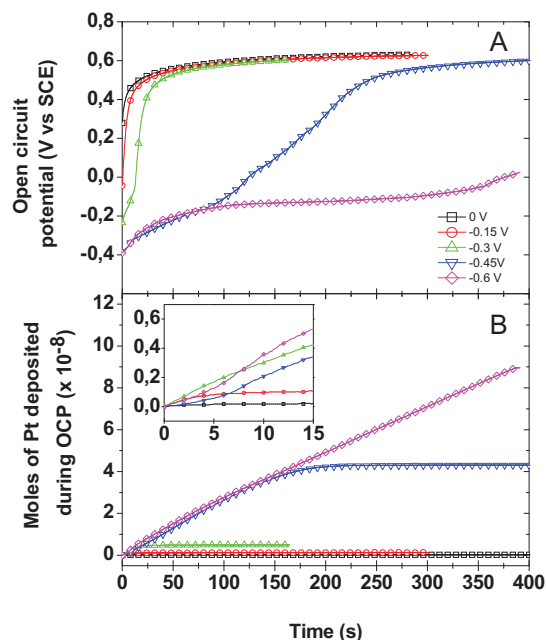


Figure 7. (Color online) Time evolution of (A) the electrode OCP and (B) the mass of the electrode following potentiostatic deposition of Pt at $V_{\text{dep}} = 0.00, -0.15, -0.30, -0.45,$ and -0.60 V on gold-plated quartz crystal. The deposition conditions were $[\text{Na}_2\text{PtCl}_6] = 5$ mM and $[\text{HCl}] = 10$ mM (KCl-free plating bath).

deposition at different values of V_{dep} is displayed, while the simultaneous evolution of the deposited mass is shown in Fig. 7B. As shown in Fig. 7A, the electrode potential increases from the initial value of V_{dep} to a limiting value close to 0.6 V. However, the time needed for the OCP to reach this limiting value increases as applied V_{dep} is made more negative. Fast recovery time (less than 30 s) of the OCP is reached for $V_{\text{dep}} \geq -0.3$ V, while it can take as long as 7 min for the most negative V_{dep} values. For $V_{\text{dep}} = -0.45$ and -0.60 V, the OCP first tends to a value ~ -0.2 V, which is close to the reversible $\text{H}_2/\text{H}_2\text{O}$ equilibrium potential. The period of time over which the OCP stays close to -0.20 V is determined by the amount of dissolved hydrogen (and thus by V_{dep}). Then, the OCP reached the equilibrium potential of the Pt^{4+}/Pt redox couple, which is 0.60 V in our conditions). Interestingly, Pt deposition still occurs during the OCP period and the number of moles of Pt deposited increases with V_{dep} . For $V_{\text{dep}} \leq -0.30$ V, the mass increase during the OCP period is attributed to the presence of H_2 that chemically reduces Pt^{4+} according to Eq. 1³⁹



In Fig. 7, the deposition of Pt is observed as long as the OCP values remained below ca. +0.20 V, which is close to the electrode potential at which hydrogen underpotential deposition occurs on Pt. This suggests that adsorbed hydrogen could also reduce Pt^{4+} according to Eq. 2. Obviously, this latter mechanism must be less important than the former one because only a monolayer of adsorbed hydrogen can be present



In this respect, a mass increase is also observed for Pt deposition performed at ca. -0.15 V, where no hydrogen is evolved (see the inset of Fig. 7B). However, the mass increase is significantly lower (i.e., 0.13×10^{-8} mol of Pt) compared to more than 4.00×10^{-8} mol for Pt deposition performed at ca. -0.45 V (cf. Fig. 7B). The mass increase during OCP period following polarization at

$V_{\text{dep}} \geq -0.3$ V could thus be attributed to Eq. 2. Indeed, considering the geometrical surface area of the crystal quartz (i.e., 0.2 cm^2), typical roughness factor of 10.0,⁴⁹ and surface density of atoms of polycrystalline Pt around ca. $1.35 \times 10^{15} \text{ atoms cm}^{-2}$,⁵⁰ one can calculate that 0.44×10^{-8} mol of adsorbed hydrogen are present on Pt (full monolayer). Considering Eq. 2 this corresponds to 0.11×10^{-8} mol of Pt adsorbed at the cathode surface. This value is in accordance with the results obtained by EQCM (cf. Fig. 7B) as 0.13×10^{-8} mol of Pt were deposited after electrode polarization at -0.15 V. It seems straightforward to conclude that NWs observed in Fig. 6B and C are more likely NTs with a Pt “stopper” at their top end, chemically deposited during the final OCP step according to Eq. 1 and 2. Therefore, the time duration of the final OCP is also a crucial parameter if one wants to synthesize (or at least observe) Pt NTs.

PtRu nanostructures.— Similar studies were performed to synthesize alloyed PtRu nanostructures, which were recently shown to exhibit interesting electrocatalytic properties,²⁸ and to demonstrate the versatility of the above-mentioned template method. Figure 8 shows SEM images of PtRu nanostructures deposited at $V_{\text{dep}} = -0.3$ V through an AAO membrane in a KCl-free plating bath. The concentrations of Na_2PtCl_6 and RuCl_3 varied from 4:1 mM to 0.5:4.5 mM and, in all cases, the total M^{2+} ion concentration remained fixed at 5 mM and the plating bath temperature was $T = 25^\circ\text{C}$ (similar to the Pt section). The morphology of the PtRu nanostructures is strongly dependent on the concentration ratios of Na_2PtCl_6 and RuCl_3 in the precursor solution. Indeed, NWs are obtained for a platinum salt concentration of 2.5 mM and higher, whereas NTs are achieved for a lower platinum salt concentration. Moreover, the interior diameter, D_i , of the NTs is also dependent on the Pt salt concentration and varies from 65 to 295 nm (resulting in thinner walls, W_i , from ca. 130 to 15 nm) as $[\text{Na}_2\text{PtCl}_6]$ varied from 1 to 0.5 mM (see Fig. 8C and D). Therefore, the formation of PtRu NTs follows the same type of behavior previously observed for pure Pt, i.e., NTs are obtained for low platinum salt concentration. Those results suggest that even in the presence of Ru salt, the key factor to achieve PtRu NTs at $V_{\text{dep}} = -0.3$ V is to limit the Pt^{4+} mass transport through the pores of the AAO membrane.

A structural analysis was performed on the PtRu deposits, and Fig. 9 shows the corresponding XRD patterns for the PtRu nanostructures depicted in Fig. 8. All the peaks can be indexed to the hexagonal phase of Ti (substrate), fcc Pt, and the hexagonal phase of Ru. The lattice parameter, a , for Pt was extracted from the XRD patterns by performing a Rietveld refinement analysis (see the inset of Fig. 9). The Pt lattice parameter decreases as one goes from 0 to 90% of RuCl_3 in the plating solution, indicating that Ru is incorporated in the Pt lattice, i.e., a PtRu alloy is formed. Hexagonal Ru is also formed for a plating bath containing more than 80% of RuCl_3 . As will be shown later on, the Ru content of those deposits exceeds 40 atom %, which corresponds to the high solubility limit of Ru in the fcc structure of Pt (Ref. 51 and references therein.)

The atomic Ru content (X_{Ru}) of the nanostructures displayed in Fig. 8A–D was evaluated by EDS and the results are presented in Fig. 10 with respect to the RuCl_3 content (X_{RuCl_3}) in the precursor solution. For comparison, PtRu films prepared on Ti substrates without the AAO membrane were also prepared in the same deposition conditions ($V_{\text{dep}} = -0.3$ V). As seen in Fig. 10, the Ru content of PtRu films follows the same trend as that observed for PtRu nanostructures, indicating that the presence of the AAO membrane does not influence the final composition of the deposit. The Ru content of the PtRu deposits is always lower than the RuCl_3 content of the solution. For example, the Ru content of the deposits is only ca. 60% for 90% of Ru metallic ions in the electrolyte. Indeed, as depicted in Fig. 2, the deposition rates of Pt and Ru are radically different and, at $V_{\text{dep}} = -0.3$ V and $T = 25^\circ\text{C}$, the deposition rate of Ru is only $\sim 15\%$ of that of Pt. So, based on these figures, one would expect the Ru content of the PtRu deposits made from an

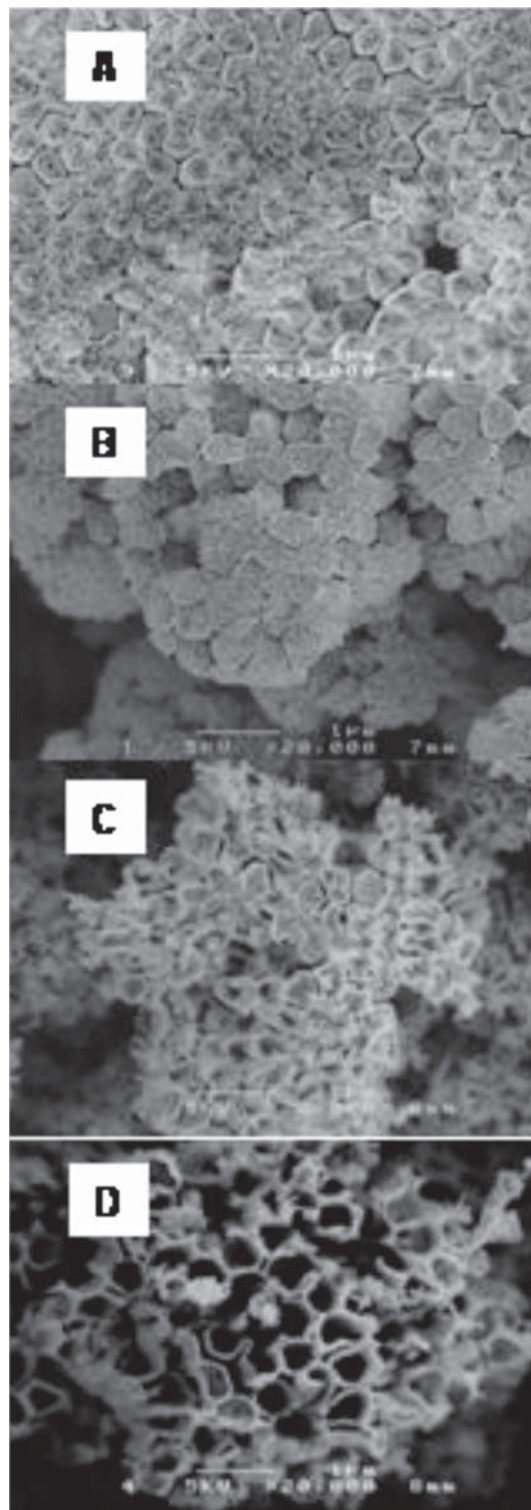


Figure 8. SEM micrographs for PtRu electrochemically deposited through an AAO membrane. The Na_2PtCl_6 : RuCl_3 concentrations are in the ratio (A) 4:1, (B) 2.5:2.5, (C) 1:4, and (D) 0.5:4.5, with $[\text{Na}_2\text{PtCl}_6] + [\text{RuCl}_3] = 5.0$ mM. In all cases, $Q_d = 40 \text{ C cm}^{-2}$, $V_{\text{dep}} = -0.3$ V, and $[\text{HCl}] = 10$ mM (KCl-free plating bath).

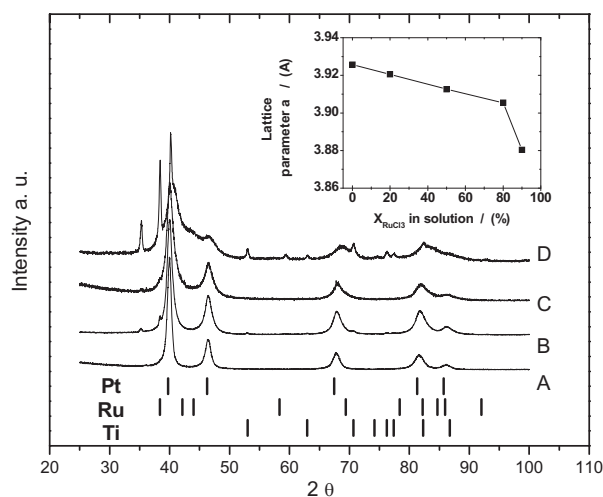


Figure 9. XRD patterns for deposits presented in Fig. 8. The inset depicts the variation of the lattice parameter a (Å) of the Pt fcc phase with respect to the proportion of RuCl_3 in the solution.

equimolar solution of Na_2PtCl_6 and RuCl_3 not to exceed 15%, which is close to the value found in Fig. 10. Therefore, the composition of PtRu deposits is consistent with the individually measured deposition rate of Pt and Ru determined by EQCM. This suggests that the composition of PtRu deposits can be determined by performing a preliminary evaluation of the deposition rate of Ru and Pt by EQCM.

Conclusion

Pt, Ru, and PtRu NWs and NTs have been achieved by a direct simple electrodeposition through an AAO membrane. NTs were obtained at high cathodic overpotential, low M^{2+} initial concentration, and low concentration of supporting electrolyte. The specific dimensions of these nanostructures (internal pore diameter and wall thickness) can be controlled by changing the cathodic overpotential and the initial metallic salt concentration. EQCM study allowed us to confirm that the growth mechanisms proposed by Fukunaka et al. (based on the coevolution of a gas during deposition), Xiao et al., and Cho and Lee (based on fast-rate, diffusion-limited deposition)

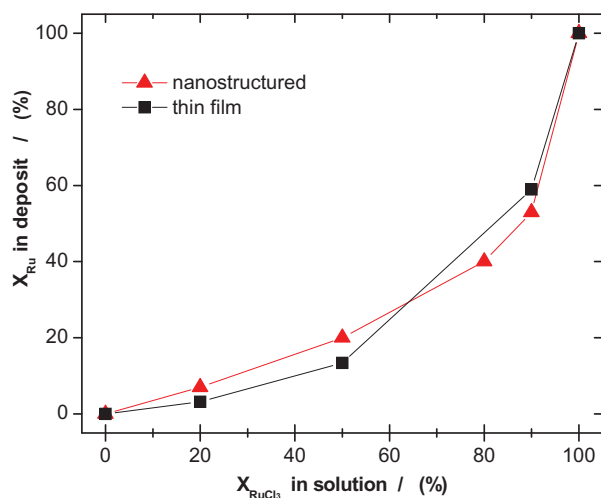


Figure 10. (Color online) Atomic concentration of Ru for deposits presented in Fig. 8 and for equivalent PtRu films prepared without an AAO membrane.

are both justified, depending on the material and the deposition conditions. Also, we have shown that NT formation is favored with a low conductivity plating bath. Moreover, NT formation can be achieved even if the porous membrane is not functionalized or if an annular conductive film is not deposited before NT formation. Finally, we showed that arrays of PtRu alloy NT and NW can be readily prepared by adjusting the composition of the electroplating bath. It is expected that electrodeposition, combined with EQCM measurements of the deposition rates, constitutes a promising tool for the synthesis of NWs and NTs of most metals, oxides, and alloys with a wide range of controlled composition and dimensions.

Acknowledgment

This work was done with the financial support of the National Science and Engineering Research Council (NSERC) of Canada and the Canada Research Chair program.

Institut National de la Recherche Scientifique assisted in meeting the publication costs of this article.

References

1. Y. Xia, P. Yang, Y. Sun, Y. Wu, B. Mayers, B. Gates, Y. Yin, F. Kim, and H. Yan, *Adv. Mater.*, **15**, 353 (2003).
2. H. J. Fan, P. Werner, and M. Zacharias, *Small*, **2**, 700 (2006).
3. Z. Chen, M. Waje, W. Li, and Y. Yan, *Angew. Chem., Int. Ed.*, **46**, 4060 (2007).
4. L. S. Van Dyke and C. R. Martin, *Langmuir*, **6**, 1118 (1990).
5. M. E. Spahr, P. Bitterli, R. Nesper, M. Muller, F. Krumeich, and H.-U. Nissen, *Angew. Chem., Int. Ed.*, **37**, 1263 (1998).
6. Y. Cui, Q. Wei, H. Park, and C. M. Lieber, *Science*, **293**, 1289 (2001).
7. M. H. Huang, S. Mao, H. Feick, H. Yan, Y. Wu, H. Kind, E. Weber, R. Russo, and P. Yang, *Science*, **292**, 1897 (2001).
8. F. Favier, E. C. Walter, M. P. Zach, T. Benter, and R. M. Penner, *Science*, **293**, 2227 (2001).
9. H. Kind, H. Q. Yan, B. Messer, M. Law, and P. D. Yang, *Adv. Mater.*, **14**, 158 (2002).
10. J. Goldberger, R. R. He, Y. F. Zhang, S. W. Lee, H. Q. Yan, H. J. Choi, and P. D. Yang, *Nature (London)*, **422**, 599 (2003).
11. M. Yun, N. V. Myung, R. P. Vasquez, C. Lee, E. Menke, and R. M. Penner, *Nano Lett.*, **4**, 419 (2004).
12. X. Quan, S. Yang, X. Ruan, and H. Zhao, *Environ. Sci. Technol.*, **39**, 3770 (2005).
13. J. H. Yuan, K. Wang, and X. H. Xia, *Adv. Funct. Mater.*, **15**, 803 (2005).
14. Y. G. Guo, J. S. Hu, H. M. Zhang, H. P. Liang, L. J. Wan, and C. L. Bai, *Adv. Mater.*, **17**, 746 (2005).
15. S.-H. Oh, R. R. Finones, C. Daraio, L. H. Chen, and S. Jin, *Biomaterials*, **26**, 4938 (2005).
16. R. Tenne, *Nat. Nanotechnol.*, **1**, 103 (2006).
17. K. Zhu, N. R. Neale, A. Miedaner, and A. J. Frank, *Nano Lett.*, **7**, 69 (2007).
18. Y. Zhang, N. Wang, S. Gao, R. He, S. Miao, J. Liu, J. Zhu, and X. Zhang, *Chem. Mater.*, **14**, 3564 (2002).
19. P. Yang and C. M. Lieber, *Science*, **273**, 1836 (1996).
20. Z. A. Peng and X. Peng, *J. Am. Chem. Soc.*, **124**, 3343 (2002).
21. Y. Sun, B. Gates, B. Mayers, and Y. Xia, *Nano Lett.*, **2**, 165 (2002).
22. S. E. Frazier, J. A. Bedford, J. Hower, and M. E. Kenney, *Inorg. Chem.*, **6**, 1693 (1967).
23. C. R. Martin, *Science*, **266**, 1961 (1994).
24. T. Chowdhury, D. P. Casey, and J. F. Rohan, *Electrochem. Commun.*, **11**, 1203 (2009).
25. H. Zhou, W. P. Zhou, R. R. Adzic, and S. S. Wong, *J. Phys. Chem. C*, **113**, 5460 (2009).
26. A. Ponrouch, S. Garbarino, M. P. Bichat, C. Maunders, G. Botton, P. L. Taberna, P. Simon, and D. Guay, *ECS Trans.*, Submitted.
27. A. Ponrouch, S. Garbarino, and D. Guay, *Electrochem. Commun.*, **11**, 834 (2009).
28. S. Garbarino, A. Ponrouch, S. Pronovost, and D. Guay, *Electrochem. Commun.*, **11**, 1449 (2009).
29. S. Garbarino, A. Ponrouch, S. Pronovost, J. Gaudet, and D. Guay, *Electrochem. Commun.*, **11**, 1924 (2009).
30. E. Antolini, T. Lopes, and E. R. Gonzalez, *J. Alloys Compd.*, **461**, 253 (2008).
31. Y. Fukunaka, M. Motoyama, Y. Konishi, and R. Ishii, *Electrochem. Solid-State Lett.*, **9**, C62 (2006).
32. R. Xiao, S. I. Cho, R. Liu, and S. B. Lee, *J. Am. Chem. Soc.*, **19**, 4483 (2007).
33. S. I. Cho and S. B. Lee, *Acc. Chem. Res.*, **41**, 699 (2008).
34. G. Sauerbrey, *Z. Phys.*, **155**, 206 (1959).
35. R. A. Young, in *The Rietveld Method*, R. A. Young, Editor, pp. 1–38, Oxford University Press, Oxford (1993).
36. A. C. Larson and R. B. Von Dreele, report no. LAUR 86-748, GSAS—General Structure Analysis System, Los Alamos National Laboratory (2000).
37. B. H. Toby, *J. Appl. Crystallogr.*, **34**, 210 (2001).
38. J. J. Jow, H. J. Lee, H. R. Chen, M. S. Wu, and T. Y. Wei, *Electrochim. Acta*, **52**, 2626 (2007).
39. P. J. Ferreira, G. J. La O', Y. Shao-Horn, D. Morgan, R. Makharia, S. Kocha, and H. A. Gasteiger, *J. Electrochem. Soc.*, **152**, A2256 (2005).
40. L. Philippe and J. Michler, *Small*, **4**, 904 (2008).

41. M. P. Zach and R. M. Penner, *Adv. Mater.*, **12**, 878 (2000).
42. H. C. Shin, J. Dong, and M. Liu, *Adv. Mater.*, **15**, 1610 (2003).
43. C. R. Martin, L. S. Van Dyke, Z. Cai, and W. Liang, *J. Am. Chem. Soc.*, **112**, 8976 (1990).
44. Y. Zhao, Y. G. Guo, Y. L. Zhang, and K. Jiao, *Phys. Chem. Chem. Phys.*, **6**, 1766 (2004).
45. L. Enze, *J. Phys. D: Appl. Phys.*, **19**, 1 (1986).
46. L. Enze, *J. Phys. D: Appl. Phys.*, **20**, 1609 (1987).
47. K. Oldham, *Electrochem. Commun.*, **6**, 210 (2004).
48. C. Amatore, A. Oleinick, and I. Svir, *Anal. Chem.*, **80**, 7947 (2008).
49. F. Vigier, F. Gloaguen, J.-M. Léger, and C. Lamy, *Electrochim. Acta*, **46**, 4331 (2001).
50. N. M. Markovic and P. N. Ross, Jr., *Surf. Sci. Rep.*, **45**, 117 (2002).
51. G. Lalonde, M. C. Denis, D. Guay, J. P. Dodelet, and R. Schulz, *J. Alloys Compd.*, **292**, 301 (1999).